Carbon Observation by Electron Energy-Loss Spectroscopy and Thermoelectric Properties of Graphite added Bismuth Antimony Telluride Prepared by Mechanical Alloying-Hot Pressing

Kenji Hirota[a], Katsuhiro Takagi[a], Kenichi Hanasaku[a], Kana L. Hasezaki[b], Hikaru Saito[c], Satoshi Hata[c,d], and Kazuhiro Hasezaki[e,*]

[a]*Graduate School of Advanced Technology and Science, Tokushima University, 2-1 Minamijiyousanjima, Tokushima 770-8506, Japan*

[b]*Interdisciplinary Graduate School of Engineering Sciences, Kyushu University, 6-1 Kasugakoen, Kasuga-shi, Fukuoka 816-8580, Japan*

[c]*Department of Advanced Materials Science and Engineering, Kyushu University, 6-1 Kasugakoen, Kasuga-shi, Fukuoka 816-8580, Japan*

[d]*The Ultramicroscopy Research Center, Kyushu University, 744 Motooka, Nishi-ku, Fukuoka 819-0395, Japan*

[e]*Graduate School of Technology, Industrial, and Social Sciences, Tokushima University, 2-1 Minamijiyousanjima, Tokushima 770-8506, Japan*

**Corresponding author: hasezaki@tokushima-u.ac.jp*

The effects of additional graphite in $(Bi_{0.3}Sb_{1.7}Te_{3.1})_{1-x}C_x$ (x = 0, 0.004, 0.012, 0.032, 0.06, and 0.12) prepared by mechanical alloying followed by hot pressing were investigated. Carbon was added to obtain a low thermal conductivity via phonon scattering. The samples were examined by X-ray diffraction, scanning electron microscopy (SEM), transmission electron microscopy (TEM), energy-dispersive X-ray spectroscopy, and electron energy-loss spectroscopy (EELS). EELS can be used to investigate the distributions of light elements such as carbon. The diffraction peaks indicated a single-phase Bi_2Te_3–Sb_2Te_3 solid solution. All the specimens were p-type semiconductors and SEM and TEM images showed dense without coarse grains. Agglomeration along the grain boundaries and inhomogeneous dispersion of carbon was observed by EELS. $(Bi_{0.3}Sb_{1.7}Te_{3.1})_{0.88}C_{0.12}$ grains wrapped by carbon layers of thickness approximately 50 nm were observed. The thermal conductivity of $(Bi_{0.3}Sb_{1.7}Te_{3.1})_{1-x}C_x$ increased with increasing x. It is considered that the presence of a large amount of carbon affected the thermal conductivity of the $Bi_{0.3}Sb_{1.7}Te_{3.1}$ matrix because the thermal conductivity of carbon is much higher than that of $Bi_{0.3}Sb_{1.7}Te_{3.1}$ and the carbon was dispersed inhomogeneously. $Bi_{0.3}Sb_{1.7}Te_{3.1}$ without additional graphite had a maximum dimensionless figure of merit ZT = 1.1. The ZT value decreased, and varied from 0.8 to 1.0, for $(Bi_{0.3}Sb_{1.7}Te_{3.1})_{1-x}C_x$. The results show that inhomogeneously dispersed carbon did not improve the thermoelectric properties of $Bi_{0.3}Sb_{1.7}Te_{3.1}$.

Keywords: A. functional alloys, B. thermoelectric properties, C. mechanical alloying and milling, D. grain boundary, F. electron energy-loss spectroscopy (EELS), G. thermoelectric power generation

1. Introduction

Thermoelectric materials have great potential for reducing fossil fuel consumption and preventing global warming because such materials enable direct conversion of thermal energy to electrical energy and reduce energy consumptions by using waste heat [1]. Energy-conversion systems based on thermoelectric materials have many advantages. They are noise free, virtually maintenance free, highly economical for long-term operation, and environmentally friendly [2,3]. Recently, many thermoelectric materials, and modules and power generation systems based on them, have been studied [4–13]. However, the thermoelectric properties of such materials need to be improved because their energy-conversion efficiencies are lower than those of other energy-conversion systems. The development of methods for improving thermoelectric properties is therefore still the main aim of much research.

The thermoelectric performance is represented by the dimensionless figure of merit *ZT*:

$$ZT = \alpha^2 \sigma \kappa^{-1} T \qquad (1)$$

where α, σ, κ, and T are the Seebeck coefficient (V K^{-1}), electrical conductivity (S m^{-1}), thermal conductivity (W m^{-1} K^{-1}), and absolute temperature (K), respectively. The thermal conductivity κ of a thermoelectric material generally consists of the phonon and carrier thermal conductivities:

$$\kappa_{\text{total}} = \kappa_{\text{phonon}} + \kappa_{\text{carrier}} = \kappa_{\text{phonon}} + L\sigma T \qquad (2)$$

where κ_{total}, κ_{phonon}, κ_{carrier}, and L are the total, phonon, and carrier thermal conductivities, and the Lorenz number of the metal (2.45×10^{-8} W S^{-1} K^{-2}), respectively [14,15].

Various intermetallics for thermoelectric materials have been extensively studied and their thermoelectric properties have been improved by using different preparation methods [16–22].

Bi_2Te_3–Sb_2Te_3-based intermetallics have been investigated because they have high *ZT* values at room temperature [23–25]. Bi_2Te_3–Sb_2Te_3-based materials can be prepared by mechanical alloying followed by hot pressing (MA–HP). MA has a grain-refining effect via grain boundary scattering. Samples are usually prepared by a powder metallurgy process such as MA to maintain a low phonon thermal conductivity. Sintered compacts prepared by MA–HP have random crystal orientations and refined structures, and these decrease the phonon thermal conductivity [26].

$Bi_{0.5}Sb_{1.5}Te_{3.0}$ prepared by melt growth has been reported to have the maximum dimensionless figure of merit *ZT* among Bi_2Te_3–Sb_2Te_3 solid solutions [27]. In recent years, it has been reported that the properties of the best undoped $Bi_{0.3}Sb_{1.7}Te_{3.0}$ material prepared by MA–HP differ from those of $Bi_{0.5}Sb_{1.5}Te_{3.0}$ prepared by melt growth [28]. It has been shown that the presence of fine grains reduces the phonon thermal conductivity of Bi_2Te_3–Sb_2Te_3 materials prepared by MA–HP compared with that of the solid solution prepared by melt growth.

The effects of doping thermoelectric materials with various elements have been widely investigated, with a view to improving their thermoelectric properties [29–35]. In a previous study, tellurium-doped $Bi_{0.3}Sb_{1.7}Te_{3.0}$, i.e., $Bi_{0.3}Sb_{1.7}Te_{3.0+x}$, was prepared by MA–HP and the effects of tellurium doping on the thermoelectric properties were investigated [36]. The properties of Bi_2Te_3–Sb_2Te_3 solid solutions are generally improved by the addition of tellurium, which acts as a carrier [37]. The doping effect is influenced by tellurium evaporation in Bi_2Te_3–Sb_2Te_3 materials because the vapor pressure of tellurium is much higher than those of bismuth and antimony [38–40]. The material obtained by addition of tellurium at $x = 0.1$, i.e., $Bi_{0.3}Sb_{1.7}Te_{3.1}$, has the maximum dimensionless figure of merit, $ZT = 1.11$, at room temperature [36].

Recently, many studies of nanostructured thermoelectric materials have been report [41–44]. For

example, carbon addition improves the thermoelectric properties of thermoelectric materials via nanoscale carbon particle dispersion [45–47]. The thermal conductivity obtained by phonon scattering is low [42,48,49], therefore phonon scattering caused by added carbon is the main reason for the improvement in the thermoelectric properties. Phonon scattering is caused by grain boundaries, and the phonon thermal conductivity is decreased by phonon scattering. As a result, the total thermal conductivity decreases, and the dimensionless figure of merit *ZT* increases. Carbon nanoparticles provide inert scattering centers for phonons in grains [48,50]. It has also been reported that carbon particles at grain boundaries prevent recrystallization and grain growth during heat treatment [45]. A low thermal conductivity can be achieved by decreasing the particle size [51,52]. Carbon particles dispersed homogenously in a $Bi_{0.3}Sb_{1.7}Te_{3.1}$ matrix increase the number of scattering centers and grain boundary scattering, and suppress grain growth, because carbon does not form compounds with bismuth, antimony, and tellurium. Carbon particle dispersion in thermoelectric materials has been investigated by energy-dispersive X-ray spectroscopy (EDS). However, it is difficult to detect carbon by this method because it is a light element and below the detection limit. In addition, graphite does not have a special shape, unlike carbon nanotubes and fullerenes, therefore graphite cannot be distinguished by its morphology. The profiles of carbon particles around grains in a matrix have therefore not been specifically reported in the literature, i.e., whether carbon particles are dispersed homogenously in the matrix. However, electron energy-loss spectroscopy (EELS) has been used to observe carbon particle dispersion. A combination of scanning transmission electron microscopy (STEM) and EELS enables analysis of light elements and chemical bonding states at high spatial resolution [53–57].

In the present study, carbon was added to a $Bi_{0.3}Sb_{1.7}Te_{3.1}$ matrix and the effects on the thermoelectric properties were evaluated. Elemental analysis and determination of the dispersion

profiles of carbon in thermoelectric materials by EELS have not been previously reported. Carbon particle dispersion in $Bi_{0.3}Sb_{1.7}Te_{3.1}$ was therefore examined by EELS, and the thermoelectric properties of the materials were investigated.

2. Experimental procedure

Bismuth (99.999%), antimony (99.9999%), tellurium (99.9999%), and carbon (graphite, 99.9%) were weighed in air to give various stoichiometries of $(Bi_{0.3}Sb_{1.7}Te_{3.1})_{1-x}C_x$ (x = 0, 0.004, 0.012, 0.032, 0.06, and 0.12). All raw materials were purchased from the Kojundo Chemical Laboratory Co., Ltd. Only millimeter-scale grains of bismuth, antimony, and tellurium were used, to decrease contamination by surface oxide layers. Graphite powder (50 μm) was used because it is more convenient than nanoscale carbon materials. The raw materials and milling medium were placed in a stainless-steel vessel in a glove box filled with Ar gas. The milling medium consisted of Si_3N_4 ceramic spheres. The vessel capacity was 0.5 L. The weight ratio of the milling medium to the raw materials was more than 20:1. Milling was performed with a Fritch P-5 planetary ball mill at a maximum rotational speed of 180 rpm for 30 h. The raw materials were converted to alloys and fine particles by MA. The graphite powder particle size decreased during MA. The milled powders were passed through a 150 μm diameter sieve, and it was confirmed that no raw materials remained. The milled powder was sintered by HP at 623 K under a uniaxial pressure of 147 MPa in an Ar atmosphere. The sintered compacts were cylinders of diameter 10 mm and height 9 mm. These compacts were cut into disks of diameter approximately 1 mm and 10 mm to obtain isotropic disks. Approximately 1 mm of the compact was removed from the top and bottom of the sintered compact surface because it has been reported that this promotes formation of the (00·l) texture [28,58].

The out-of-plane direction of the sintered disks were examined by X-ray diffraction (XRD; Rigaku SmartLab) with Cu Kα radiation. All the sintered disks were examined in the Bragg angle range 2θ =

20° to 90°, with a step size of 0.1° and a step speed of 5.0 s per step.

The microstructures and elemental dispersions in cross-sections of the sintered disks (x = 0.06 and 0.12) were investigated by scanning electron microscopy (SEM; JEOL, JSM-6510A) and EDS (Super-X), respectively. Transmission electron microscopy (TEM; Titan Cubed G2 60-300 C_s-corrected S/TEM) was used to determine the grain sizes of the sintered disks (x = 0 and 0.12). Carbon particle dispersion in the sintered disks (x = 0.06 and 0.12) was investigated by a combination of STEM and EELS (Gatan Quantum 965).

The thermal and electrical conductivities, and the Seebeck coefficients at room temperature of all the disks were determined using laboratory-constructed systems. The thermal conductivities were determined by static comparison methods [27,29,59]. The material used for comparison in the static comparisons was quartz (κ = 1.411 W m^{-1} K^{-1}). The electrical conductivities were determined by the four-point probe method using a delta mode electrical resistance system based on a 2182A/6220 instrument (Keithley Instruments, Inc.) The probe was of size 1.0 mm and made of tungsten carbide. All measurements made using the electrical conductivity system were confirmed by ohmic contact [29]. The Seebeck coefficients were determined using the constructed thermal contact method, and confirmed by measurements using the standard reference material SRM3451 [30,60]. The accuracies of the electrical and thermal conductivities were less than ±1% and that of the Seebeck coefficient was less than ±2%.

3. Results and discussion

Fig. 1 shows the XRD patterns of sintered disks of $(Bi_{0.3}Sb_{1.7}Te_{3.1})_{1-x}C_x$ (x = 0, 0.004, 0.012, 0. 032, 0.06, and 0.12) prepared by MA–HP. The main indexes of a Bi_2Te_3–Sb_2Te_3 solid solution are shown. All the diffraction peaks indicate a single-phase Bi_2Te_3–Sb_2Te_3 solid solution. The characteristic diffraction peaks corresponding to carbon were not observed, despite the presence of added carbon.

These results show that carbon did not react with $Bi_{0.3}Sb_{1.7}Te_{3.1}$ and had no effect on the XRD pattern of the $Bi_{0.3}Sb_{1.7}Te_{3.1}$ matrix.

Fig. 2(a) shows a STEM bright field micrograph of a $(Bi_{0.3}Sb_{1.7}Te_{3.1})_{0.94}C_{0.06}$ sintered disk prepared by MA–HP, and Fig. 2(b)–(e) show the STEM-EDS results for bismuth, antimony, tellurium, and carbon, respectively. All the sintered disks consisted of dense grains without coarse grains. Fig. 2(a)–(c) show that bismuth, antimony, and tellurium were homogeneously dispersed in $(Bi_{0.3}Sb_{1.7}Te_{3.1})_{0.94}C_{0.06.}$ Although homogenous dispersion of carbon is also likely, this cannot be observed in Fig. 2(e), probably because most of the characteristic X-rays from carbon were absorbed by the $Bi_{0.3}Sb_{1.7}Te_{3.1}$ matrix.

Fig. 3(a) and (b) show a STEM annular dark field image and EELS carbon mapping, respectively, of a $(Bi_{0.3}Sb_{1.7}Te_{3.1})_{0.94}C_{0.06}$ sintered disk prepared by MA–HP. The observed area is the same as that in Fig. 2. The white region in Fig. 3(b) indicates carbon and shows that carbon agglomerates are present in the $(Bi_{0.3}Sb_{1.7}Te_{3.1})_{0.94}C_{0.06}$ sintered disk. Carbon particle were not clearly observed in the grain of the $(Bi_{0.3}Sb_{1.7}Te_{3.1})_{0.94}C_{0.06}$.

Carbon was inhomogeneously dispersed in the $(Bi_{0.3}Sb_{1.7}Te_{3.1})_{0.94}C_{0.06}$ matrix, and $Bi_{0.3}Sb_{1.7}Te_{3.1}$ grains were wrapped in carbon layers of thickness approximately 50 nm. This result is completely different from that obtained by EDS carbon elemental mapping, shown in Fig. 2(e).

Fig. 4(a) shows a SEM micrograph of a cross-section of a $(Bi_{0.3}Sb_{1.7}Te_{3.1})_{0.88}C_{0.12}$ sintered disk prepared by MA–HP, and Fig. 4(b)–(e) show the EDS results for bismuth, antimony, tellurium, and carbon. The carbon elemental mapping in Fig. 4(e) indicates homogeneous dispersion of carbon particles in the matrix. However, most of the characteristic X-rays from carbon were absorbed by the $Bi_{0.3}Sb_{1.7}Te_{3.1}$ matrix. The elemental mapping of bismuth (Fig. 4b) shows that bismuth segregation only occurred for $x = 0.12$. This might be because bismuth telluride, which was formed at $x = 0.12$,

gave bismuth segregation by reaction with a large quantity of carbon containing impurity contamination during sintering.

Fig. 5 shows a STEM bright field image of a $(Bi_{0.3}Sb_{1.7}Te_{3.1})_{0.88}C_{0.12}$ sintered disk prepared by MA–HP. The approximate grain size varied from 400 nm to 1 μm. The grain size of the undoped $Bi_{0.3}Sb_{1.7}Te_{3.1}$ sintered disk was approximately the same. This shows that the carbon particles did not significantly affect the matrix grain size. These STEM images do not show agglomeration and homogenous dispersion of carbon.

Fig. 6(a) and (b) show a STEM annular dark field image and EELS carbon mapping, respectively, of a $(Bi_{0.3}Sb_{1.7}Te_{3.1})_{0.88}C_{0.12}$ sintered disk prepared by MA–HP. As in Fig. 5(b), the white region in Fig. 6(b) indicates carbon, and carbon agglomeration along the grain boundary can be observed. The carbon in $(Bi_{0.3}Sb_{1.7}Te_{3.1})_{0.88}C_{0.12}$ was inhomogeneously dispersed. Fig. 3 shows $Bi_{0.3}Sb_{1.7}Te_{3.1}$ grains wrapped in carbon layers of thickness approximately 50 nm. Carbon particles were not clearly observed in the grains of the $(Bi_{0.3}Sb_{1.7}Te_{3.1})_{0.88}C_{0.12}$ sintered disk. The EELS results shown in Figs. 5 and 6 differ from those obtained by EDS analysis. It is considered that the carbon particle dispersion profile cannot be observed by EDS because most of the characteristic X-rays from carbon were absorbed by the $Bi_{0.3}Sb_{1.7}Te_{3.1}$ matrix. It is therefore difficult to distinctly observe both agglomeration and homogenous dispersion of carbon by using EDS. However, EELS analysis enables the observation and determination of light elements such as carbon. In the present study, carbon elemental mapping was clearly achieved by EELS.

Fig. 7 shows the total (κ_{total}), phonon (κ_{phonon}), and carrier ($\kappa_{carrier}$) thermal conductivities of $(Bi_{0.3}Sb_{1.7}Te_{3.1})_{1-x}C_x$ at room temperature. The total thermal conductivity increased slightly with increasing carbon addition. The phonon thermal conductivity increased with increasing carbon addition. These results are contrary to our expectations. We suggest that the thermal conductivity of

$Bi_{0.3}Sb_{1.7}Te_{3.1}$ increased with increasing carbon addition because the thermal conductivity of carbon (graphite) is much higher than that of $Bi_{0.3}Sb_{1.7}Te_{3.1}$ ($\kappa_{graphite}$ = 100 W m^{-1} K^{-1} [61]). In addition, the grain sizes of $(Bi_{0.3}Sb_{1.7}Te_{3.1})_{1-x}C_x$ were almost the same as that of $Bi_{0.3}Sb_{1.7}Te_{3.1}$. Additional carbon did not prevent grain growth by agglomeration and inhomogeneous dispersion of carbon particles during hot pressing.

Fig. 8 shows plots of the electrical conductivity versus x for $(Bi_{0.3}Sb_{1.7}Te_{3.1})_{1-x}C_x$ at room temperature. For $x \leq 0.06$, the electrical conductivity decreased with increasing carbon addition. Similarly to the case for the thermal conductivity, we suggest that the electrical conductivity of carbon affects that of $Bi_{0.3}Sb_{1.7}Te_{3.1}$ because the electrical conductivity of carbon is lower than that of $Bi_{0.3}Sb_{1.7}Te_{3.1}$ (σ = 7.3 × 10^4 S m^{-1} [61]), i.e., carbon acts as a conductive material in $Bi_{0.3}Sb_{1.7}Te_{3.1}$ because of agglomeration and inhomogeneous dispersion of carbon, which were observed by STEM-EELS (see Fig. 6). However, the electrical conductivity increased at x = 0.12. This indicates that the segregation of bismuth observed by EDS affects the semiconductor properties of $(Bi_{0.3}Sb_{1.7}Te_{3.1})_{0.88}C_{0.12}$. The constituent elements probably act as dopants and the electrical conductivity increases because of bismuth segregation (see Fig. 4).

Fig. 9 shows plots of the Seebeck coefficient versus x for $(Bi_{0.3}Sb_{1.7}Te_{3.1})_{1-x}C_x$ at room temperature. For $x \leq 0.06$, the Seebeck coefficient remained constant. This indicates that carbon addition had no effect on the Seebeck coefficient of $Bi_{0.3}Sb_{1.7}Te_{3.1}$. This is probably because bismuth, antimony, and tellurium do not form compounds with carbon. However, the Seebeck coefficient at x = 0.12 decreased slightly more than the measurement error (±2%). This is consistent with the electrical conductivity at x = 0.12 because there is an inverse relationship between the Seebeck coefficient α and the electrical conductivity σ based on the carrier balance [62]. These results suggest that bismuth segregation affects the Seebeck coefficient.

Fig. 10 shows plots of the dimensionless figure of merit ZT versus x for $(Bi_{0.3}Sb_{1.7}Te_{3.1})_{1-x}C_x$ at room temperature. At $x = 0$, the maximum dimensionless figure of merit, $ZT = 1.1$, was obtained. At $0.004 \leq x \leq 0.06$, ZT varied from 0.8 to 1.0.

These results show that the thermoelectric properties of $Bi_{0.3}Sb_{1.7}Te_{3.1}$ were not improved by inhomogeneously dispersed carbon. This is probably because inhomogeneous dispersion of carbon did not lower the thermal conductivity. The results suggest that agglomeration and inhomogeneous dispersion of carbon particles prevented the achievement of a low thermal conductivity and improvement of the thermoelectric properties of $Bi_{0.3}Sb_{1.7}Te_{3.1}$.

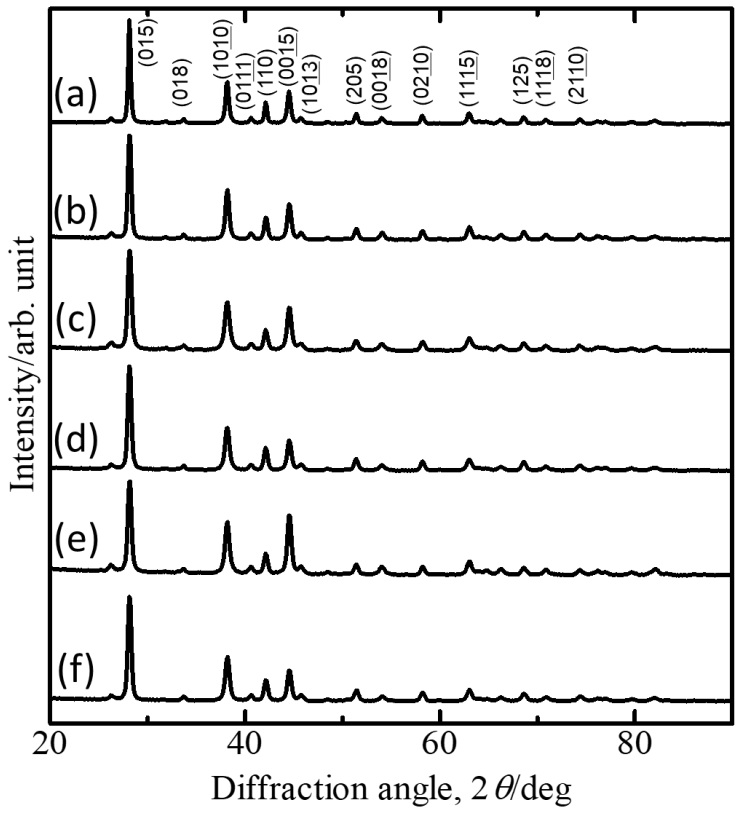

Fig. 1 XRD patterns (2θ = 20° to 90°) of $(Bi_{0.3}Sb_{1.7}Te_{3.1})_{1-x}C_x$ sintered disks prepared by MA–HP, with x = (a) 0, (b) 0.004, (c) 0.012, (d) 0.032, (e) 0.06, and (f) 0.12. Main indexes for Bi_2Te_3–Sb_2Te_3 are shown.

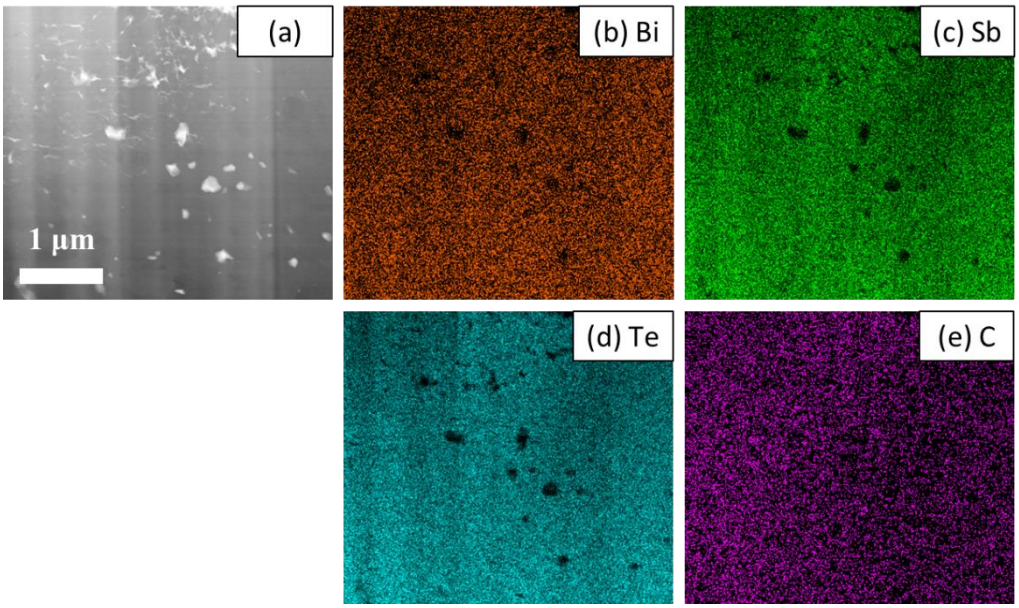

Fig. 2 (a) STEM bright field micrograph and EDS analysis of (b) bismuth, (c) antimony, (d) tellurium, and (e) carbon for $(Bi_{0.3}Sb_{1.7}Te_{3.1})_{0.94}C_{0.06}$ sintered disk prepared by MA–HP.

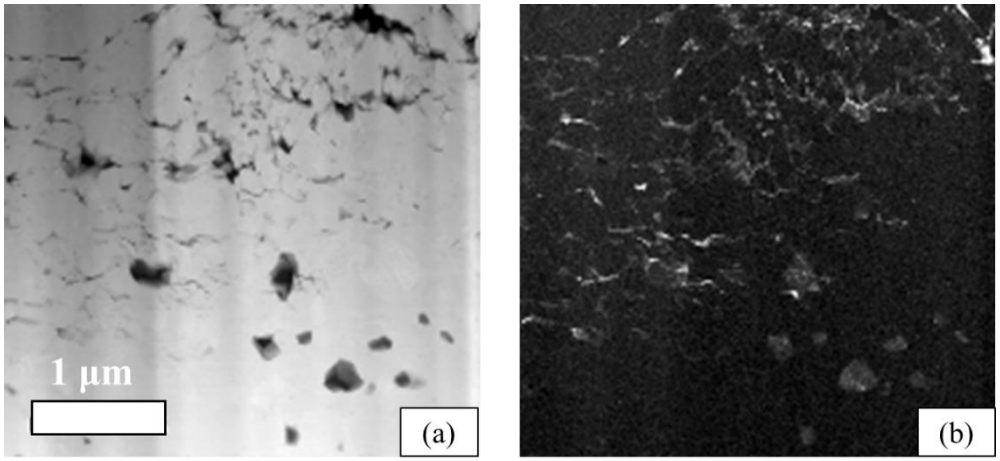

Fig. 3 (a) STEM annular dark field image and (b) EELS carbon mapping of $(Bi_{0.3}Sb_{1.7}Te_{3.1})_{0.94}C_{0.06}$ sintered disk prepared by MA–HP.

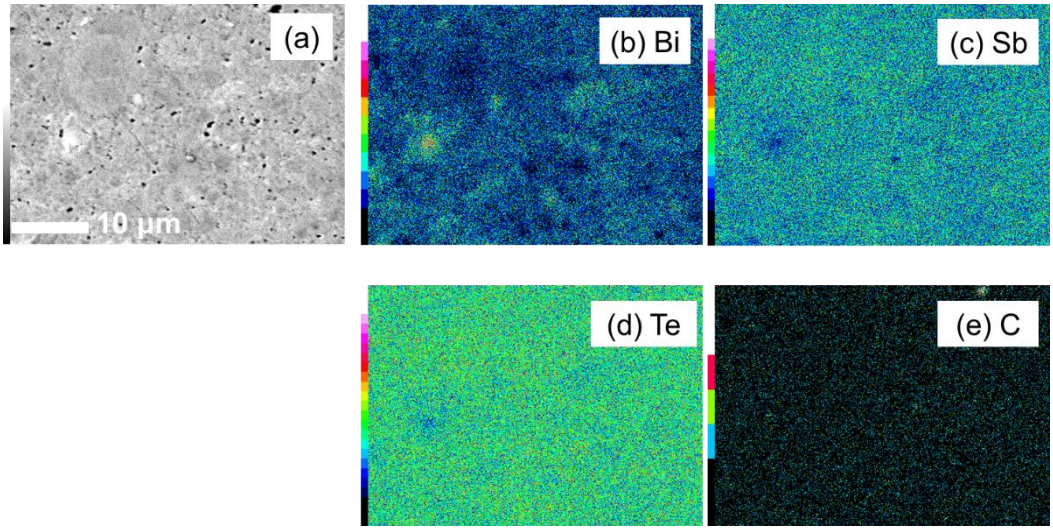

Fig. 4 (a) SEM micrograph of cross-section and EDS analysis of (b) bismuth, (c) antimony, (d) tellurium, and (e) carbon for $(Bi_{0.3}Sb_{1.7}Te_{3.1})_{0.88}C_{0.12}$ sintered disk prepared by MA–HP.

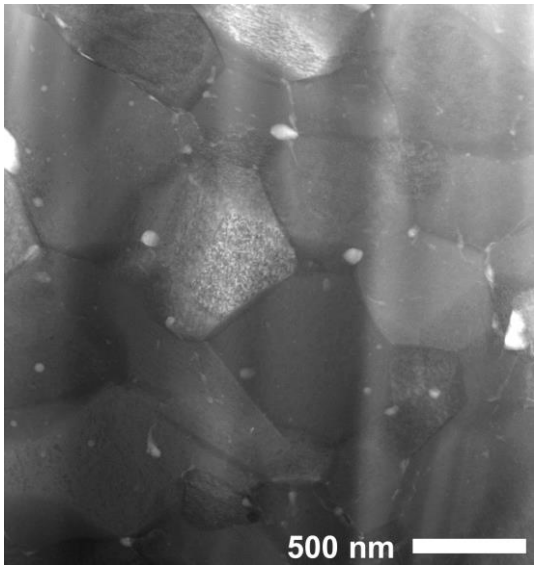

Fig. 5 STEM bright field image of $(Bi_{0.3}Sb_{1.7}Te_{3.1})_{0.88}C_{0.12}$ sintered disk prepared by MA-HP.

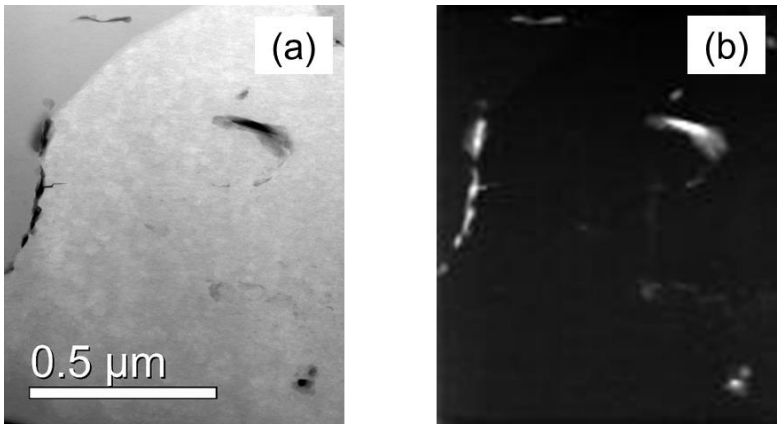

Fig. 6 (a) STEM annular dark field image and (b) EELS carbon mapping of $(Bi_{0.3}Sb_{1.7}Te_{3.1})_{0.88}C_{0.12}$ sintered disk prepared by MA–HP.

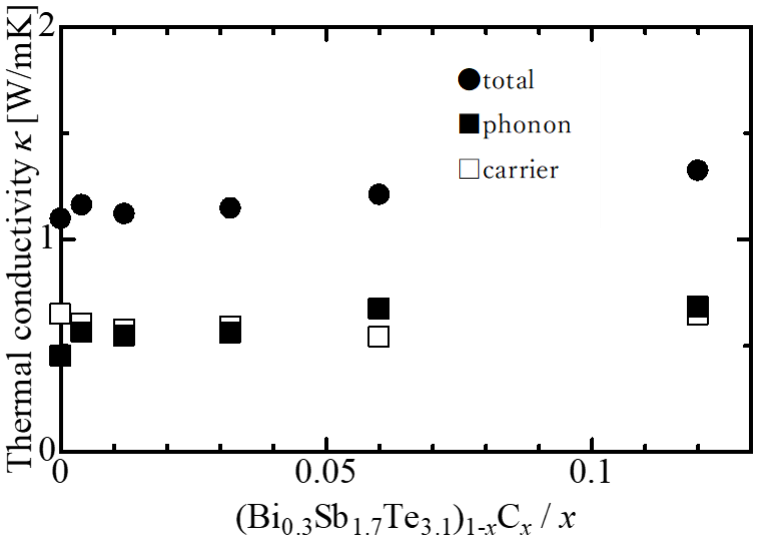

Fig. 7 Thermal conductivity versus x for $(Bi_{0.3}Sb_{1.7}Te_{3.1})_{1-x}C_x$ at room temperature.

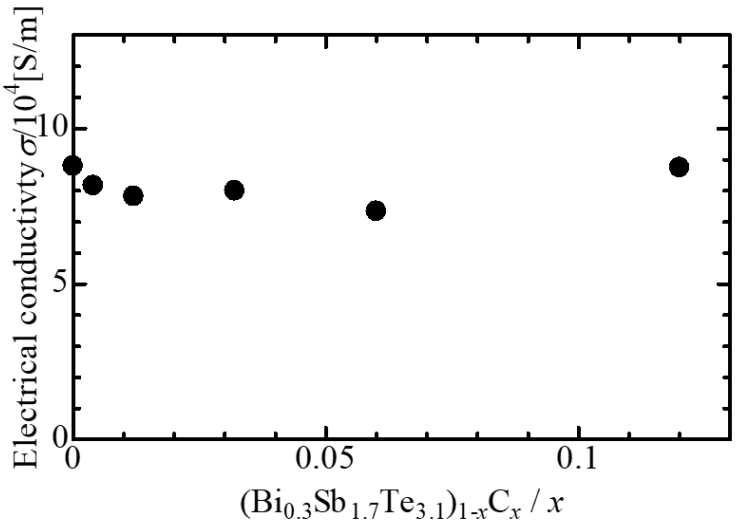

Fig. 8 Electrical conductivity versus x for $(Bi_{0.3}Sb_{1.7}Te_{3.1})_{1-x}C_x$ at room temperature.

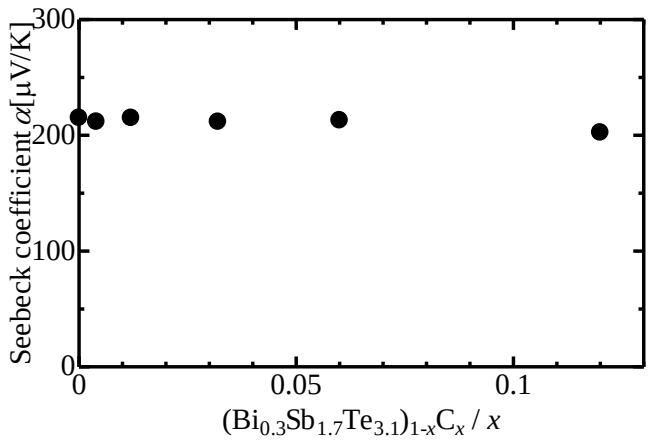

Fig. 9 Seebeck coefficient versus x for $(Bi_{0.3}Sb_{1.7}Te_{3.1})_{1-x}C_x$ at room temperature

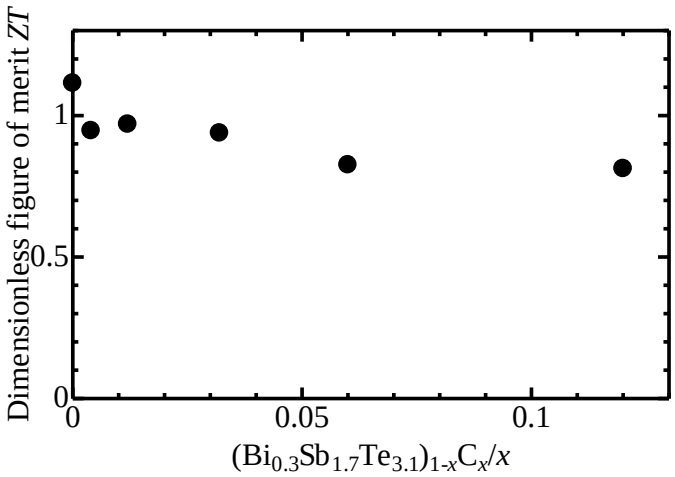

Fig. 10 Dimensionless figure of merit ZT versus x for $(Bi_{0.3}Sb_{1.7}Te_{3.1})_{1-x}C_x$ at room temperature.

4. Conclusions

In the present study, the effects of additional carbon in $(Bi_{0.3}Sb_{1.7}Te_{3.1})_{1-x}C_x$ (x = 0, 0.004, 0.012, 0.032, 0.06, and 0.12) prepared by MA–HP were investigated. The results are summarized as follows.

(1) SEM showed that all the specimens consisted of dense grains, without coarse grains. The approximate grain size for the $(Bi_{0.3}Sb_{1.7}Te_{3.1})_{0.88}C_{0.12}$ sintered disk varied from 400 nm to 1 μm.

(2) Carbon dispersion profiles were not clearly observed by EDS. However, agglomeration and inhomogeneous dispersion of carbon along the grain boundaries of the $Bi_{0.3}Sb_{1.7}Te_{3.1}$ matrix were observed by STEM-EELS.

(3) The $Bi_{0.3}Sb_{1.7}Te_{3.1}$ grains were wrapped by carbon layers of thickness approximately 50 nm. Carbon particles were not clearly observed in the grain of $(Bi_{0.3}Sb_{1.7}Te_{3.1})_{1-x}C_x$ sintered disk.

(4) The thermal conductivity of $(Bi_{0.3}Sb_{1.7}Te_{3.1})_{1-x}C_x$ increased slightly with increasing x. This is because the thermal conductivity of carbon is much higher than that of $Bi_{0.3}Sb_{1.7}Te_{3.1}$.

(5) For $Bi_{0.3}Sb_{1.7}Te_{3.1}$ without additional carbon the dimensionless figure of merit ZT was 1.1. For $0.004 \leq x \leq 0.12$, the dimensionless figure of merit ZT for $(Bi_{0.3}Sb_{1.7}Te_{3.1})_{1-x}C_x$ varied from 0.8 to 1.0.

Acknowledgements

This work was supported by JSPS KAKENHI Grant Number JP17K06863. We thank Helen McPherson PhD, from Edanz Group (www.edanzeditng.com/ac) for editing a draft of this manuscript.

References

[1] D.M. Rowe, Introduction, in: D.M. Rowe (Ed.), CRC Handb. Thermoelectr., CRC press Inc, 1995: pp. 1–3.

[2] T. Kajikawa, Thermoelectric Power Generation System Recovering Industrial Waste Heat, in: D.M. Rowe (Ed.), Thermoelectr. Handb. Macro to Nano, CRC press, 2006.

[3] O. Umezawa, Y. Shinohara, K. Halada, New Aspects of Ecomaterials from the Viewpoints of the Consumer and Regional Communities, Mater. Trans. 55 (2014) 745–749. doi:10.2320/matertrans.MB201302.

[4] L.C. Terry M. Tritt, Böttner Harald, Thermoelectrics : Direct Solar Thermal Energy Conversion, MRS Bull. 33 (2008) 366–368. doi:10.1557/mrs2008.73.

[5] G. Skomedal, L. Holmgren, H. Middleton, I.S. Eremin, G.N. Isachenko, M. Jaegle, K. Tarantik, N. Vlachos, M. Manoli, T. Kyratsi, D. Berthebaud, N.Y. Dao Truong, F. Gascoin, Design, assembly and characterization of silicide-based thermoelectric modules, Energy Convers. Manag. 110 (2016) 13–21. doi:10.1016/j.enconman.2015.11.068.

[6] H. Al-Madhhachi, G. Min, Effective use of thermal energy at both hot and cold side of thermoelectric module for developing efficient thermoelectric water distillation system, Energy Convers. Manag. 133 (2017) 14–19. doi:10.1016/j.enconman.2016.11.055.

[7] Y. Takagiwa, Y. Sato, A. Zevalkink, I. Kanazawa, K. Kimura, Y. Isoda, Y. Shinohara, Thermoelectric properties of $EuZn_2Sb_2$ Zintl compounds: zT enhancement through Yb substitution for Eu, J. Alloys Compd. 703 (2017) 73–79. doi:10.1016/j.jallcom.2017.01.350.

[8] Y. Shinohara, The State of the Art on Thermoelectric Devices in Japan, Mater. Today Proc. 2 (2015) 877–885. doi:10.1016/j.matpr.2015.05.114.

[9] D. Ben-Ayoun, Y. Sadia, Y. Gelbstein, High temperature thermoelectric properties evolution of $Pb_{1-x}Sn_xTe$ based alloys, J. Alloys Compd. 722 (2017) 33–38. doi:10.1016/j.jallcom.2017.06.075.

[10] Y. Gelbstein, $Pb_{1-x}Sn_xTe$ Alloys : Application Considerations, J. Electron. Mater. 40 (2011) 533–536. doi:10.1007/s11664-010-1435-6.

[11] D.M. Rowe, G. Min, Evaluation of thermoelectric modules for power generation, J. Power Sources. 73 (1998) 193–198.

[12] G. Min, D.M. Rowe, Cooling performance of integrated thermoelectric microcooler, Solid. State. Electron. 43 (1999) 923–929.

[13] O. Beeri, O. Rotem, E. Hazan, E.A. Katz, A. Braun, Y. Gelbstein, Hybrid photovoltaic-thermoelectric system for concentrated solar energy conversion : Experimental realization and modeling, J. Appl. Phys. 118 (2015) 115104. doi:10.1063/1.4931428.

[14] H.J. Goldsmid, Springer Seres in Materials Science 121 Introduction to Thermoelectricity, in: H.J. Goldsmid (Ed.), Springer-Verlag, Belrin, 2010: p. 31.

[15] M. Stordeur, Valence Band Structure and the Thermoelectric Figure-of-Merit of $(Bi_{1-X}Sb_X)_2Te_3$ Crystals, in: D.M. Rowe (Ed.), CRC Handb. Thermoelectr., CRC press Inc, 1995: p. 241.

[16] Y. Isoda, S. Tada, N. Shioda, Y. Shinohara, Si-particle-size dependence of Mg_2Si powders

directly produced by liquid-solid synthesis method, J. Alloys Compd. 656 (2016) 598–603. doi:10.1016/j.jallcom.2015.07.291.

[17] Y. Takagiwa, Y. Isoda, M. Goto, Y. Shinohara, Electronic structure and thermoelectric properties of narrow-band-gap intermetallic compound $Al_2Fe_3Si_3$, J. Therm. Anal. Calorim. 131 (2018) 281–287. doi:10.1007/s10973-017-6621-9.

[18] S.K. Singh, Y. Isoda, M. Imai, Synthesis and thermoelectric properties of the quaternary type-I Si clathrates $K_{8-\delta}Ga_xAl_ySi_{46-x-y}$, Intermetallics. 82 (2017) 93–100. doi:10.1016/j.intermet.2016.11.006.

[19] G. Rogl, P. Rogl, Skutterudites, a most promising group of thermoelectric materials, Curr. Opin. Green Sustain. Chem. 4 (2017) 50–57. doi:10.1016/j.cogsc.2017.02.006.

[20] P. Sauerschnig, A. Grytsiv, J. Vrestal, V. V Romaka, B. Smetana, G. Giester, E. Bauer, P. Rogl, On the constitution and thermodynamic modelling of the system, J. Alloys Compd. 742 (2018) 1058–1082. doi:10.1016/j.jallcom.2017.12.012.

[21] B. Madavali, H. Kim, K. Lee, Y. Isoda, F. Gascoin, S. Hong, Large scale production of high efficient and robust p-type Bi-Sb-Te based thermoelectric materials by powder metallurgy, JMADE. 112 (2016) 485–494. doi:10.1016/j.matdes.2016.09.089.

[22] Y. Shiota, H. Muta, K. Yamamoto, Y. Ohishi, K. Kurosaki, S. Yamanaka, A new semiconductor $Al_2Fe_3Si_3$ with complex crystal structure, Intermetallics. 89 (2017) 51–56. doi:10.1016/j.intermet.2017.05.019.

[23] D.M. Rowe, General Principles and Basic Considerations, in: D.M. Rowe (Ed.), Thermoelectr. Handb. Macro to Nano, CRC press, 2006.

[24] X. Wang, Y. Li, G. Liu, F. Shan, Intermetallics Achieving high power factor of p-type BiSbTe thermoelectric materials via adjusting hot-pressing temperature, Intermetallics. 93 (2018) 338–342. doi:10.1016/j.intermet.2017.10.015.

[25] R.O.I. Vizel, T.A.L. Bargig, O. Beeri, Y. Gelbstein, Bonding of Bi_2Te_3-Based Thermoelectric Legs to Metallic Contacts Using $Bi_{0.82}Sb_{0.18}$ Alloy, J. Electron. Mater. 45 (2016) 1296–1300. doi:10.1007/s11664-015-4003-2.

[26] K. Hasezaki, M. Nishimura, M. Umata, H. Tsukuda, M. Araoka, Mechanical Alloying of BiTe and BiSbTe Thermoelectric Materials, Mater. Trans. 35 (1994) 428–432.

[27] K. Uemura, I. Nishida, Thermoelectric Semiconductor and its Applications, in: Nikkankougyou Shinbunsha, Tokyo, 1988: pp. 168–169, 195–197.

[28] M. Kitamura, K. Hasezaki, Effect of Mechanical Alloying on Thermal Conductivity of Bi_2Te_3-Sb_2Te_3, Mater. Trans. 57 (2016) 2153–2157.

[29] K. Hasezaki, S. Wakatsuki, T. Fujii, Constituent Element Addition to *n*-Type $Bi_2Te_{2.67}Se_{0.33}$ Thermoelectric Semiconductor without Harmful Dopants by Mechanical Alloying, Mater. Trans. 57 (2016) 1001–1005.

[30] M. Fusa, N. Yamamoto, K. Hasezaki, Measurement of Seebeck coefficient and conductive behaviors of $Bi_2Te_{3-x}Se_x$ (x=0.15-0.6) thermoelectric semiconductors without harmful dopants, Mater. Trans. 55 (2014) 942–946.

[31] Y. Gelbstein, J. Davidow, Highly efficient functional $Ge_xPb_{1-x}Te$ based thermoelectric alloys, Phys. Chem. Chem. Phys. 16 (2014) 20120–20126. doi:10.1039/c4cp02399d.

[32] F. Failamani, P. Broz, D. Maccio, S. Puchegger, H. Müller, L. Salamakha, H. Michor, A. Grytsiv,

A. Saccone, E. Bauer, G. Giester, P. Rogl, Intermetallics Constitution of the systems {V,Nb,Ta}-Sb and physical properties of di-antimonides {V,Nb,Ta}Sb_2, Intermetallics. 65 (2015) 94–110. doi:10.1016/j.intermet.2015.05.006.

[33] S. Maier, S. Ohno, G. Yu, S.D. Kang, T.C. Chasapis, V.A. Ha, S.A. Miller, D. Berthebaud, M.G. Kanatzidis, G.-M. Rignanese, G. Hautier, G.J. Snyder, F. Gascoin, Resonant Bonding, Multiband Thermoelectric Transport, and Native Defects in n-Type $BaBiTe_{3-x}Se_x$ (x = 0, 0.05, 0.1), Chem. Mater. 30 (2018) 174–184. doi:10.1021/acs.chemmater.7b04123.

[34] V.N. Kumar, Y. Hayakawa, H. Udono, Y. Inatomi, Enhanced thermoelectric properties of InSb: Studies on In/Ga doped GaSb/InSb crystals, Intermetallics. 105 (2019) 21–28. doi:10.1016/j.intermet.2018.11.006.

[35] E. Hazan, N. Madar, M. Parag, V. Casian, O. Ben-Yehuda, Y. Gelbstein, Effective Electronic Mechanisms for Optimizing the Thermoelectric Properties of GeTe-rich Alloys, Adv. Electron. Mater. 11 (2015) 1500228.

[36] K. Hirota, M. Kitamura, K. Takagi, K. Hasezaki, Thermoelectric Behaviors of $Bi_{0.3}Sb_{1.7}Te_{3.0}$ with Excess or Deficiency of Tellurium Prepared by Mechanical Alloying Followed by Hot Pressing, Mater. Trans. 59 (2018) 1233–1238.

[37] H. Scherrer, S. Scherrer, Thermoelectric properties of bismuth antimony telluride solid solution, in: D.M. Rowe (Ed.), CRC Handb. Macro to Nano, CRC press Inc, Florida, 2006.

[38] R. Cohen, D.R. Lide, G.L. Trigg, AIP Physics Desk References, in: R. Cohen, D.R. Lide, G.L. Trigg (Eds.), 3rd ed., Springer-Verlag, New York, 2003: pp. 831–833.

[39] Y. Suga, Netsudenhanndoutai, in: Makisyoten, Tokyo, 1966: p. 317.

[40] H. Zou, D.M. Rowe, G. Min, Growth of p- and n-type bismuth telluride thin films by co-evaporation, J. Cryst. Growth. 222 (2001) 82–87.

[41] M.S. Dresselhaus, G. Chen, M.Y. Tang, R. Yang, H. Lee, D. Wang, Z. Ren, J.P. Fleurial, P. Gogna, New Directions for Low-Dimensional Thermoelectric Materials, Adv. Mater. 19 (2007) 1043–1053. doi:10.1002/adma.200600527.

[42] B. Poudel, Q. Hao, Y. Ma, Y. Lan, A. Minnich, B. Yu, X. Yan, D. Wang, A. Muto, D. Vashaee, X. Chen, J. Liu, Mildred S. Dresselhaus, G. Chen, Z. Ren, High-Thermoelectric Performance of Nanostructured Bismuth Antimony Telluride Bulk Allys, Science (80-.). 320 (2008) 634–638. doi:10.1126/science.1155140.

[43] M. Martín-González, O. Caballero-Calero, P. Díaz-Chao, Nanoengineering thermoelectrics for 21st century: Energy harvesting and other trends in the field, Renew. Sustain. Energy Rev. 24 (2013) 288–305. doi:10.1016/j.rser.2013.03.008.

[44] K. Kirievsky, Y. Orr, A. O'Neill, D. Fuks, Y. Gelbstein, Peculiarities of doping of nanograined thermoelectric TiNiSn by 3d noble and transition metals, Intermetallics. 98 (2018) 154–160. doi:10.1016/j.intermet.2018.05.003.

[45] Q. Lognoné, F. Gascoin, On the effect of carbon nanotubes on the thermoelectric properties of n-$Bi_2Te_{2.4}Se_{0.6}$made by mechanical alloying, J. Alloys Compd. 635 (2015) 107–111. doi:10.1016/j.jallcom.2015.02.055.

[46] B. Trawiński, B. Bochentyn, N. Gostkowska, M. Łapiński, T. Miruszewski, B. Kusz, Structure and thermoelectric properties of bismuth telluride—Carbon composites, Mater. Res. Bull. 99 (2018) 10–17. doi:10.1016/j.materresbull.2017.10.043.

[47] W. Hu, H. Zhou, X. Mu, D. He, P. Ji, W. Hou, P. Wei, W. Zhu, X. Nie, W. Zhao, Preparation and

Thermoelectric Properties of Graphite/$Bi_{0.5}Sb_{1.5}Te_3$ Composites, J. Electron. Mater. 47 (2017) 3344–3349. doi:10.1007/s11664-017-5908-8.

[48] H. Nagai, K. Nagai, S. Katsuyama, K. Majima, Thermoelectric Properties of $FeSi_2$ with SiC Dispersion Prepared by Mechanical Alloying, J. Japan Soc. Powder Powder Metall. 43 (1996) 608–612.

[49] S.A. Humphry-Baker, C.A. Schuh, Anomalous grain refinement trends during mechanical milling of Bi_2Te_3, Acta Mater. 75 (2014) 167–179. doi:10.1016/j.actamat.2014.04.032.

[50] H. Nagai, Effects of Mechanical Alloying and Grinding on the Preparation and the Thermoelectric Properties of β-$FeSi_2$, Mater. Trans. 36 (1995) 365–372. doi:10.2320/matertrans1989.36.365.

[51] J. Yoshino, Theoretical estimation of thermoelectric figure of merit in sintered materials and proposal of grain-size-graded structures, Funct. Graded Mater. (1996) 495–500.

[52] Cronin B. Vining, Thermoelectric properties of pressure-sintered $Si_{0.8}Ge_{0.2}$, J. Appl. Phys. 69 (1991) 331–341.

[53] R.F. Egerton, M. Malac, EELS in the TEM, J. Electron Spectros. Relat. Phenomena. 143 (2005) 43–50. doi:10.1016/j.elspec.2003.12.009.

[54] H. Saito, S. Mizuma, N. Yamamoto, Confinement of Surface Plasmon Polaritons by Heterostructures of Plasmonic Crystals, Nano Lett. 15 (2015) 6789–6793. doi:10.1021/acs.nanolett.5b02623.

[55] H. Saito, N. Yamamoto, Control of Light Emission by a Plasmonic Crystal Cavity, Nano Lett. 15 (2015) 5764–5769. doi:10.1021/acs.nanolett.5b01719.

[56] H. Saito, N. Yamamoto, T. Sannomiya, Waveguide Bandgap in Crystalline Bandgap Slows Down Surface Plasmon Polariton, ACS Photonics. 4 (2017) 1361–1370. doi:10.1021/acsphotonics.6b00943.

[57] T. Sannomiya, H. Saito, J. Junesch, N. Yamamoto, Coupling of plasmonic nanopore pairs: Facing dipoles attract each other, Light Sci. Appl. 5 (2016) 1–7. doi:10.1038/lsa.2016.146.

[58] M. Orihashi, Y. Noda, K. Hasezaki, Surface texture of Bi_2Te_3-based materials deformed under pressure-current heating, in: Proc. 2007 Int. Conf. Thermoelectr., Cheju, Korea, 2007: pp. 95–98.

[59] T.M. Tritt, Thermal Conductivity Theory, Properties, and Applications, in: Plenum Publishers, New York, 2004: pp. 9–17, pp. 193–195.

[60] N.D. Lowhorn, W. Wong-Ng, Z.Q. Lu, E. Thomas, M. Otani, M. Green, N. Dilley, J. Sharp, T.N. Tran, Development of a Seebeck coefficient Standard Reference Material, Appl. Phys. A Mater. Sci. Process. 96 (2009) 511–514. doi:10.1007/s00339-009-5191-5.

[61] T. Watanabe, Encyclopedia of the Elements, in: Asakura Publishing Co., Ltd, Tokyo, 2007: pp. 478–479.

[62] C.M. Bhandari, D.M. Rowe, Optimization of Carrier Concentration, in: D.M. Rowe (Ed.), CRC Handb. Thermoelectr., Press, CRC, Taylor & Francis Group, Boca Raton, Florida, 1995: pp. 43–44.